RSC Publishing Faraday Discussions

Imaging the behavior of molecules in biological systems: Breaking the 3D speed barrier with 3D Multi-resolution Microscopy

Journal:	*Faraday Discussions*
Manuscript ID:	FD-ART-05-2015-000090
Article Type:	Paper
Date Submitted by the Author:	22-May-2015

Complete List of Authors:	Welsher, Kevin; Princeton University, Chemistry Yang, Haw; Princeton University, Chemistry Department

Imaging the behavior of molecules in biological systems: Breaking the 3D speed barrier with 3D Multi-resolution Microscopy

Kevin Welsher[†] and Haw Yang[*]
Department of Chemistry, Princeton University, New Jersey, USA

Abstract

The overwhelming effort in the development of new microscopy methods has been focused on increasing the spatial and temporal resolution in all three dimensions to enable the measurement of the molecular scale phenomena at the heart of biological processes. However, there exists a significant speed barrier to existing 3D imaging methods which is associated with the overhead required to image large volumes. This overhead can be overcome to provide nearly unlimited temporal precision by simply focusing on a single molecule or particle via real-time 3D single-particle tracking and the newly developed 3D Multi-resolution Microscopy (3D-MM). Here, we investigate the optical and mechanical limits of real-time 3D single-particle tracking in the context of other methods. In particular, we investigate the use of an optical cantilever for position sensitive detection, finding that this method yields system magnifications of over 3000x. We also investigate the ideal PID control parameters and their effect on the power spectrum of simulated trajectories. Taken together, these data suggest that the speed limit in real-time 3D single particle-tracking is a result of slow piezoelectric stage response as opposed to optical sensitivity or PID control.

Introduction

Imaging is an attempt to capture a static snapshot of the contents of a scene. When a scene is dynamically changing, several snapshots, or frames, are taken in rapid succession to capture the progression of a temporally evolving event. At the macroscale, our ability to capture dynamic events is limited in the spatial domain primarily by the size and number of pixels in our detector, while the temporal resolution is dictated by how frequently frames can be read out. With the development of high resolution and high speed cameras, nearly any macroscopic event can be captured, from the rupturing of a balloon to the exploding of a bullet from the barrel of a gun.

Imaging in live cell microscopy is aimed at capturing the state and dynamics of cellular behavior. At the heart of these cellular scale events are molecules, such as proteins, small molecule co-factors and nucleic acids, whose dynamics and interactions lead to all cellular and organism level function. At these microscales, we encounter many of the same obstacles as macroscale imaging, with a couple of added challenges. First, spatial resolution ceases to be limited by the pixel density of our detector, but rather by the diffractive nature of light, which limits the resolvability of objects to about half the wavelength light used, meaning that structures below ~ 200 nm cannot be resolved with light from the visible spectrum[1] and that we cannot rely on simple scattering or reflection of light to follow a specific molecule, but need specific labeling strategies so that only the molecule of interest yields a signal while others do not. As a result, live cell imaging has relied heavily on fluorescence labeling to follow specific molecular details, despite existing in a sea of other unlabeled molecules. Live cell microscopy also suffers from limited temporal resolution. The reliance on fluorescence, where a single molecule may only yield a few thousand photons per second, has led to longer integration times and slower "frame rates". At the same time, narrow depth of field has commonly been overcome by stacking several

[†] Current address: Department of Chemistry, Duke University, Durham, North Carolina 27708 (kevin.welsher@duke.edu)
[*] hawyang@princeton.edu

images together at different focal planes, further reducing the temporal resolution. The combined lack of spatial, temporal and 3D resolution has long hampered our ability to observe molecular phenomena on their native length scale (down to <1 nm) and on a time scale relevant to molecular dynamics (sub-millisecond), while simultaneously placing these interactions and dynamics in their macromolecular biological context. The traditional methods of observing molecular biology in context have been optical imaging methods, starting with the most predominantly used and commercially available method: confocal microscopy.

Scanning Methods

Confocal fluorescence microscopy, as originally implemented,[2-4] Current laser scanning microscopes (LSMs) implement resonant galvanic scanners, which can easily achieve video rate scans of a single optical section.[5] However, imaging in LSMs is still fundamentally limited by the amount of time the scanner spends on a particular pixel (the pixel dwell time). As the scan rate increases, the pixel dwell time drops. For example, when sampling a 512x512 image at 1 Hz, the pixel dwell time is about 4 μsec, assuming zero time for mirror flyback. To achieve video rate (30 Hz), the dwell time becomes 133 nsec, drastically reducing the signal to noise in each pixel. Today, LSMs based on resonant scanners can achieve modest signal-to-noise 3D volumes on the order of 0.1 volumes-per-second (VPS).[6] To overcome these short pixel dwell times, a parallelized approach was needed. Confocal microscopes have been further improved by the implementation of Nipkow spinning disks.[7] These high speed confocal units have really pushed the limits of confocal microscopy, allowing rendering of 3D volumes at up to 1 VPS,[8] with near confocal performance.[9] While the spinning disk method allows faster imaging, it is a difficult method to implement, as the pinhole array is constructed for a particular objective (typically 100x, NA=1.4), making switching to larger length scales difficult. Moreover, these time scales (≥1 second) are far too slow to monitor chemical dynamics at the cellular or subcellular level.

Due to the optical diffraction limit, the smallest resolvable features visible to confocal microscopes are on the order of 200 nm in the lateral dimensions and 600 nm in the axial dimensions.[1] Early attempts to increase the spatial resolution of these microscopes included the addition of an additional detection/excitation objective to increase the solid angle covered by the microscope and to effectively reduce the point-spread function (PSF) of the system. This "4Pi" microscopy[10] increased the axial resolution of a confocal microscope down to ~100 nm.[11] Other methods have sought to bypass the diffraction limit entirely. Nonlinear methods, such as stimulated emission depletion microscopy (STED)[12] and reversible saturable optical fluorescence transitions (RESOLFT)[13] use shaped excitation pulses to effectively turn off fluorescence emission in a certain area. By carefully shaping the laser pulse to define a spherical area with a node of zero intensity at the focal spot, the focal spot size can be effectively reduced in size due to the depletion of surrounding emission. In RESOLFT, photoswitchable probes are set to their dark state everywhere except in a small dub-diffraction region around the focus. In STED, the depletion pulse promotes stimulated emission to the point that the excited state lifetime is zero and there is a very low chance of spontaneous emission. Both of these approaches have been extremely successful in surpassing the diffraction limit, with STED reaching isotropic focal spots with resolution down to 30 nm, enabling imaging mitochondrial cristae in live cells.[14]

While all of these point-scanning methods have made huge leaps in the ability to resolve biological features approaching the molecular scale, they carry certain limitations when it comes to placing these phenomena in the context of larger scale biological processes, such as in multicellular organisms. For point scanning methods observing large scales necessarily means trading off for slower observation times, especially when the super-resolution voxels necessitate extremely small step sizes. For instance, high speed STED imaging has been achieved with frame rates up to 28 Hz, but only for very small imaging areas (2.5 μm x 1.8 μm).[15] This video rate temporal resolution is quickly lost when the observation area needs to be expanded. This

has been begun to be addressed by using massively parallelized STED,[16] though this method still requires a few hundred camera frames per image, which precludes it from being used for high-speed 3D imaging. Similar improvements have been made in RESOLFT, achieving a super-resolved image of a 120 μm x 100 μm field of view in less than 1 second.[17] Of course, these imaging rates will be greatly decreased as these methods are scaled to 3 dimensions.

Super-resolution localization methods

Other methods have relied on localization of single fluorophores. Despite the limitations of optical microscopes, the location of single fluorophores can be known with great precision. The image of a fluorophore, which is effectively a point source, is a Gaussian profile which is determined by the PSF of the objective lens. The spread of the profile is determined by the diffraction limit, but the precision with which the center of the distribution can be measured is determined by the number measurements that are made on the molecule of interest. Given enough photons and perfect instrumentation, the location of a single molecule can be known down to nanometer resolution.[18,19] The difficulty with applying this method to real biological systems is the difficulty in locating a single molecule among many. Several methods have aimed at solving this problem using blinking or photoswitchable probes. Sparse sets of these fluorohores are imaged in a sample repeatedly until the full image is reconstructed. These methods (stochastic optical reconstruction microscopy, STORM[20]; fluorescence photoactivated localization microscopy, PALM[21] and fPALM[22]) have shown the ability to resolve phenomena down to the 10s of nm scale

While these methods were initially implemented for investigating phenomena in two dimensions, they have been extended to three dimensions via a variety of different methods. One method is the so-called astigmatic imaging, which uses a cylindrical lens to deliberately skew the PSF such that the image of a single molecule changes as a function of defocus (STORM, 20-30 nm lateral, 60 nm axial).[23,24] Other methods have relied on the simultaneous imaging of two focal planes (biplane imaging, BP-PALM, 30 nm lateral, 75 nm axial)[25] or interferometry (iPALM, 20 nm lateral, 10 nm axial).[26] Perhaps the most successful approach implemented thus far is the double helix PSF (DH-PSF, 10 nm lateral, 10 nm axial),[27] which uses a spatial light modulator or phase mask to encode 3D information into the PSF of a single emitter. Unfortunately, all of these efforts to extend these single molecule approaches to three dimensions suffer from limited range. While the astigmatism, biplane and double helix PSF methods have proven to be great methods for gathering high resolution axial localization data without requiring scanning optical slices, they come with the drawback that they only maintain their precision over 1-2 microns at the most,[28] severely limiting extension to larger structures. Further work on the SLM or phase mask approach has extended this range to the 5-6 micron range.[29] However, as these PSFs become more complex, the molecules in each frame will need to be separated by greater and greater distances for individual spots to be identified. On the temporal side, these approaches require the observation of many switching events to isolate individual fluorophores, which initially limited their temporal resolution to 10s or more per image. Recent advances, however, have shown improved temporal sampling, down to 1-2 seconds per image.[30,31] Ultimately, the advent of faster imaging sCMOS based cameras will improve this limited temporal sampling, which has already shown the potential to achieve 32 frames per second.[32]

Rapid volumetric imaging

Several methods have aimed to solve the problem of imaging large 3D volumes with high temporal resolution. One of these methods is selective plane illumination microscopy (SPIM).[33] This method uses an excitation beam that is spread out by a cylindrical lens and delivered to the sample perpendicular to the collection objective, creating a plane of illumination which allows for optical sectioning. Fast imaging of

volumes of 400 x 400 x 200 um of neuronal action potentials every 6 seconds have been achieved.[34] The axial resolution of this method is unfortunately limited by the spread of the excitation beam, on the order of 5 microns. This method has been improved by rapidly scanning a laser beam to create an illumination plane, allowing for more intense illumination and faster acquisition times, acquiring volumes of 1000 x 1000 x 600 um in 60 – 90 seconds with 300 nm lateral and 1000 nm axial resolution.[35,36] More recently, Hillman and colleagues have taken a different approach, using a rotating polygonal mirror to scan a volume at high speed, showing the ability to achieve 3D imaging in at up to 10 volumes per second.[37] However, these methods are still "cellular" scale, which may have great promise in studying organism level behavior, will struggle to study the behavior of molecules.

Probably the most impressive rapid volumetric imaging achieved to date has been the so-called "Bessel-beam" approach. This approach overcomes the limited axial resolution of the SPIM approach by using a narrow excitation beam created using an annular transmission mask and a low magnification objective lens which is perpendicular to the observation objective. This narrow excitation beam is then scanned through the sample to generate a 3D image. The implementation of this Bessel beam with two-photon excitation enables axial resolution down to 500 nm.[6] Impressively, entire cellular processes can be observed at rates approaching 1 volume per second.[38]

Possibly the most well established super-resolution method which aims to combine the benefits of super-resolution with larger scale observations is the structured illumination microscope (SIM).[39] By implementing excitation fields with frequencies near the spatial frequencies of the sample, a lower beat frequency, observable by a traditional microscope objective, can be created. This method has shown the ability to improve the lateral resolution down to ~110 nm and axial resolution down to ~350 nm.[40,41] 3D-SIM has been improved to achieve 0.25 VPS in single color and 0.11 VPS in two color imaging. These speeds have been far surpassed by a completely analog version, wherein the need to collect 10-100 digital images per optical sections is eliminated, allowing 100 Hz imaging in two dimensions.[42]

Despite efforts to push for higher temporal and spatial resolution in microscopy, there is still a huge range of length and time scales that go unobserved. Figure 1 shows a representative resolution/scale plot for the temporal and spatial capabilities of several of the methods above. The plot shows the resolution of each method, both spatial and temporal as well as the spatial "scale", or the spatial extent over which imaging is possible. For each method, the best spatial and temporal resolution for 3D measurements was chosen, with spatial resolution taken from the worst of lateral or axial resolution. The spatial scale was selected given the results for the highest frame rates achieved for each method. Here, we have omitted characterization of the temporal scale, as this is difficult to compare without comparing all methods at similar conditions to account for photobleaching, toxicity, etc. In the upper right corner of the plot, we find the traditional point scanning methods. Moving to the left (towards greater spatial resolution) we find the "super-resolution" methods. For instance, the single molecule methods such as DH-PSF and iPALM show remarkable spatial resolution, as illustrated by their circles on the left hand side of the plot. In the lower right hand side, we have the rapid volumetric imaging methods, which have achieved some improvement in their temporal resolution, but still have relatively limited spatial resolution.

When plotting the data in this way there is a noticeable lack of methods which approach the native spatial and temporal scales of molecular interactions (nanometer and microsecond respectively). Upon inspection, the reason for this lack is obvious: imaging an entire scene carries far too much observational overhead to allow for the capturing of the sub-millisecond dynamics of a single molecule. This can be thought of as the inverse of the scaling problem observed in LSM or other point scanning methods. When increasing the

spatial scale of our observation, by necessity, the temporal resolution will suffer from the increased data overhead at a given spatial resolution. Given this reasoning, it is easy to imagine that unlimited temporal sampling can be achieved in the limit of extremely small spatial scale and short exposure time. Effectively, if we want to understand the dynamics of a molecule with the highest possible precision, we should focus solely on that molecule.

To address this shortcoming, we developed a new hybrid implementation where the high spatial and temporal resolution real-time 3D single-particle tracking[43-46] is combined with the large-scale contextual information of a conventional two-photon scanning fluorescence microscope. This method, called 3D Multi-resolution Microscopy (3D-MM) is a breakthrough in correlating fast subcellular dynamics in a larger cellular context.[47] 3D-MM is implemented through the spectral separation and data synchronization of two imaging modalities: a real-time 3D single-particle tracking module and a two-photon LSM. The real-time 3D single particle-tracking module locks quickly moving particles in the focus of the objective via a piezoelectric stage and an optical feedback loop running at 100 kHz. The repeated centroid measurement of the particle at high rate results in spatial resolution down to 10-20 nm, placing it on the left hand side of Fig. 1. Further, the high sampling rate imparts time resolution of 10 μs, a vast improvement over other methods. The reason for this improved temporal resolution is straightforward. Focusing solely on a single probe in the focal volume of the objective and disregarding contextual resolution leads to an extremely narrow spatial scale. The spatial scale is essentially equal to the spatial resolution. As a result, real-time 3D single particle tracking is able to best super-resolution methods in terms of combined spatial and temporal resolution, but is incapable of placing these high resolution measurements in a larger scale biological context. In simpler terms, the highest possible spatiotemporal precision can be achieved by discarding all observational overhead, with no measurement of the areas around the particle. Combining this real-time measurement of a single probe with large scale context provided by the two-photon LSM yielded the first fully resolved, real-time 3D data of an extracellular nanoparticle approaching and landing on the cell surface. The power of the 3D-MM to address multiple spatiotemporal scales is demonstrated in Figure 3. Fluorescently labeled 100 nm nanoparticles labeled with the TAT peptide[48] were prepared as described in Ref. 47 and allowed to bind to the surface of fluorescent protein labeled NIH-3T3 cells. The 3D-MM technique allows simultaneous observation of the larger cellular environment via the two-photon LSM (Fig. 3a,b) while recording the real-time 3D position of the nanoparticle at 100 kHz. By tracing the particle's position, the isotropic precision (<15 nm in XYZ) carves out 3D sub-diffraction structures such as hemispherical and cylindrical membrane protrusions which are unresolvable by conventional imaging methods (Fig. 3c,d). Data like these could be revolutionary to the fields of virology and drug delivery.

3D-MM is a powerful technique which is able to bridge multiple spatiotemporal scales in a single method, which is a necessity in the evaluation of molecular dynamics in biological systems. Critical to the application of the 3D-MM technique is the capacity to follow single particles in real-time in three dimensions with high precision. The ability to follow diffusive particles is dependent on two factors. First, there must be an optical readout of the particle's position which is sensitive to very small changes. Second, there needs to be a sufficiently fast response mechanism to keep the particle in the focus of the objective. By keeping the particle in the small focal volume, we can use single point detectors and achieve near unlimited temporal resolution, as shown in Fig. 2.

Optical Response

While the optical feedback differs with each implementation,[43-47,49-51] each real-time 3D single-particle tracking method relies on getting position sensitive detection of the particle to be tracked with high temporal

resolution. The simplest way one can think of doing this is to magnify the image of the particle onto a position sensitive detector. The largest challenge here is achieving large enough magnification such that the detector is sensitive to nanometer scale displacements of the particle in real-time. For a typical high magnification system (e.g. 100x), a 1 nm displacement of a particle will only result in a 100 nm displacement of the particle image given a standard tube lens configuration. If this signal is split onto different detectors, there may not be sufficient signal to noise to detect this difference. To achieve higher magnification, the most straightforward approach is the use a lens pair after the microscope tube lens in order to increase the total system magnification. For example, a combination of a 75 mm and a 750 mm lens pair following the tube lens would result in a further 10x magnification, bringing the total system magnification to 1000x. However, this results in a detection mechanism which would change greatly with defocus of the target particle. As the goal is 3D particle tracking, we do not want our ability to track in X or Y to be affected by the ability to track in Z. The elegant solution to this problem is the optical cantilever.[45,46]

The optical cantilever delivers nanometer resolution to real-time 3D single-particle tracking by optically converting nanometer linear displacements of the target into angular variations, which at large distances become discernable shifts in the projected images. The mechanism behind the optical cantilever is similar to that of the lens pair magnification suggested above, without the final long focal length lens (above: 750 mm). Instead of focusing the particle's image onto the position sensitive detector, the infinity space projection of the particle's image is split, in this case using a prism mirror, onto two different detectors. The principle is shown in the cartoon inset of Figure 4. As the particle is displaced in the object plane by a distance **Δ**, the angle with which the light exits the objective back aperture is deflected by an angle θ, given by the relation:

$$\tan(\theta) = \left(\frac{\Delta}{f_{obj}}\right) \cdot \left(\frac{f_{tube}}{f_{cantilever}}\right) \qquad (1)$$

Where $\mathbf{f_{obj}}$, $\mathbf{f_{tube}}$ and $\mathbf{f_{cantilever}}$ are the focal lengths of the object lens, tube lens and optical cantilever lens, respectively. The offset, **d**, of the infinity space output of the optical cantilever is then given by:

$$\tan(\theta) = \frac{d}{L} \qquad (2)$$

Where **L** is the length of the optical cantilever, which is the distance between the cantilever lens and the prism mirror. Substituting for **tan(θ)** yields:

$$d = \left(\frac{\Delta}{f_{obj}}\right) \cdot \left(\frac{f_{tube}}{f_{cantilever}}\right) \cdot L \qquad (3)$$

The ratio of **L** to $\mathbf{f_{cantilever}}$ can be thought of as an effective magnification in addition to the magnification from the ratio of the tube lens to the objective lens focal lens. The offset of the infinity space beam at the prism mirror is linearly proportional to the length of the optical cantilever, meaning to increase the optical resolution of the tracking system, one only needs to increase the distance between the optical cantilever lens and the position sensitive detector. As an illustrative example, the recent implementation of 3D-MM used a 100X Zeiss Plan Apo (NA =1.4, $\mathbf{f_{obj}}$ = 1.65 mm), a 200 mm tube lens and a 75 mm optical cantilever lens to track 100 nm fluorescent nanoparticles.[47] For a particle displacement of 1 nm, the simple magnification of the objective and tubes lens (Mag ≈ 121x) results in a image offset of 121 nm. However, given an optical cantilever length of 2 meters, this 1 nm displacement becomes a 3.2 μm image offset, yielding an effective magnification of 3200x.

The effect of the optical cantilever on the simulated optical response of the position sensitive detectors is shown in Figure 4. To model the optical system response, a point source of 500 nm wavelength light (FWHM ≈

268 nm) is imaged onto the prism mirror via the optical cantilever. The point source is imaged onto the intermediate image plane via the tube lens, which is then projected into infinity space by the optical cantilever lens. It should be noted that the optical cantilever lens serves two purposes here. First, as described above, it magnifies the angular displacement of the parallel bundle of rays exiting the microscope. Second, and almost as significantly, the optical cantilever lens serves to shrink the bundle of rays. This means that for a given displacement at the prism mirror, the optical response will be even greater due to the smaller size of the infinity space Gaussian beam, which in this case has FWHM ≈ 1 mm if divergence is neglected. The process variable (**PV**) that is used for real-time tracking can be calculated by splitting this infinity space beam onto two perfectly integrating detectors as a function of particle displacement in the object plane. Figure 4 shows the resulting calculation of this error function for a range of different optical cantilever lengths, ranging from 100 mm to 100 m. While cantilever lengths of 10 m or greater are experimentally untenable, they serve as a guide to the ultimate limit of this approach. At short cantilever lengths (100 mm), the optical error function is almost perfectly linear over at least 2 μm in the object space, but the position readout is shallow, with a slope of ~ $3 \cdot 10^{-4}$ nm^{-1}. In the other extreme, an optical cantilever of 100 m would yield a control slope of ~ 0.2 nm^{-1}, but would only be linear over a distance of about 8 nm. In practice, it is found that an optical cantilever length of about 2 m gives the best results for real-time 3D single-particle tracking. Under this model, this distance should yield a control slope of $4.3 \cdot 10^{-3}$ nm^{-1} over a range of at about half a micron.

Despite the simplicity of the model used above to predict the optical response as a function of optical cantilever length, it agrees quite well with experimentally measured values. To compare the predicted control to the real system, 110 nm fluorescent beads (Tetraspeck, Life Technologies) were scanned by a piezoelectric stage (MadCity Labs Nano-LPQ). The beads were excited with a 642 nm diode laser (Coherent Cube) operating at ~ 5 μW in the focus of a 100x Zeiss Plan Apo objective. Fluorescence was collected through the same objective and focused by a 200 mm achromatic doublet tube lens (Thorlabs) onto the intermediate image plane. The intermediate image was projected at infinity by a 75 mm achromatic doublet. After a distance of ~ 2 m, the collimated output from the 75 mm cantilever lens was split by a prism mirror. The resulting split images were focused by 45 mm achromats (Thorlabs) onto two single photon counting APDs (Excelitas SPCM-AQRH-13). The particle was scanned in 100 nm steps and fluorescence was collected by both APDs for a period of 10 ms. The process variable (**PV**) is calculated as the difference of the intensity of the two detectors divided by their sum:

$$PV = \frac{I_1 - I_2}{I_1 + I_2} \qquad (4)$$

The result of the particle scan is shown in Figure 5 (green circles), along with the predicted control for a 2 m optical cantilever (red line). The two curves show remarkably good agreement near the focus, with nearly identical control slopes. The main differences between the two curves likely arise from the difference between the actual experimental setup and the simplified calculation. First of all, the experiment relies on real detectors with small (~ 180 μm) active areas. As a result, the detector may not collect all the photons as the particle displaces further and further from the prism mirror center. This, along with the presence of non-zero background (dark counts and background scattering), preclude the experimental process variable from reaching ±1 at the extremes of particle displacement. Secondly, the calculated slope seems to slightly outperform the experimental realization. This is likely due to not accounting for beam divergence over the length of the optical cantilever. Even in the case of small divergence, the infinity beam will become wider at the prism mirror than in the divergence-free case, resulting in a slightly reduced control slope.

In addition to lateral position sensing, change in the axial position of the particle must also be measured in real-time with high precision. This can be achieved by imaging the particle onto an offset confocal pinhole with a short focal length lens (here f = 2.9 mm). As in typical confocal microscopy, objects which lie above or below the optical section defined by the pinhole will yield a lower signal. Displacing the confocal pinhole away from the focus of the tracked particle allows a nearly linear index into the particle's position. Figure 6 shows the predicted optical tracking response for 5, 10 and 15 micron pinholes at various displacements from the objective's focal volume. For all three pinholes tested, there is a flat response at small displacements (< 0.5 μm in the object space), followed by a rapid drop in the Z process variable, which is the Z-detector readout ($\mathbf{I_z}$) after normalization to the XY detectors discussed above for the optical cantilever ($\mathbf{I_x + I_y}$). While the 5 μm pinhole yields the sharpest control slope, it also restricts light collection to the highest degree. The 15 μm pinhole has higher throughput, but shallower control. The 10 μm pinhole shows a good intermediate response. For comparison, the simulated 10 μm pinhole response is compared to an experimentally measured scan of a fluorescent particle as described above. In this case, the particle is scanned through the objective's focal volume in the Z-direction.

Feedback Control

The optical response is only one factor which governs the performance of real-time 3D single particle tracking microscopies. Detecting deviations in the particle's position at high speeds are only half the battle. The other half of the challenge is active feedback control to maintain the particle in the focal volume of the objective, which is what ultimately allows extremely high sampling rates (as allowed due to the small spatial scale, see Fig. 2). Generally, this feedback control is applied using optical position sensitive detection, proportional-integral-derivative (PID) control[52] and high-speed, 3D piezoelectric stages. The process variable from the optical readout is converted to an analog voltage as dictated by the PID control parameters and fed to the stage to move the sample and maintain the tracked particle in the focal volume of the objective lens.

Both the PID control parameters and the response speed and accuracy of the piezoelectric stage contribute to the ultimate limits of real-time 3D single-particle tracking. In general PID control, the control applied to maintain a certain setpoint in a system is governed by the following equation:

$$C_i = K_P \cdot err_i + K_I \cdot \sum_{n=0}^{i} err_n + K_D \cdot \left(PV_i - PV_{i-1}\right) \qquad (5)$$

where $\mathbf{C_i}$ is the control signal to be applied, $\mathbf{K_P}$, $\mathbf{K_I}$ and $\mathbf{K_D}$ are the proportional, integral and derivative control weights. $\mathbf{K_P}$ operates purely on the current state of the system, $\mathbf{K_I}$ operates on the integrated state of the system over time and $\mathbf{K_D}$ operates on the recent change of the system. The system error, **err**, is defined as follows:

$$err_i = SP - PV_i \qquad (6)$$

SP is the setpoint that is the maintained by the control loop and **PV** is the current state of the system. In the case of the optical cantilever detection described above, the goal is to keep the particle's image centered with respect to the prism mirror. This occurs when both detectors have the same reading and the error function will have a value of zero (as in Figs. 4 and 5). This means that to maintain the particle in the center of the focus of the objective lens, **SP** is set to 0. As the particle is displaced away from the center, the **PV** will take on a nonzero value which will be used as the input for PID control.

While there are a number of approximate methods for predicting the values of the control weights, they are routinely optimized based on the response of the system to the control. In this case, the control weights are chosen based on which yield the longest trajectories on the most quickly diffusing particles. Here, we develop a

simple methodology for predicting the values of the control weights and show the results for one dimension. First, 1D trajectories of 60 nm diffusing particles are generated with 10 μsec step sizes. Then, a simulated control algorithm is applied which uses the empirically measured optical response function for the 2 m optical cantilever detection described above. The output of the simulated control is run through a 500 Hz low pass filter, which simulates the behavior of the piezoelectric stage. This low-pass filter is a good approximation for the piezoelectric stage for two reasons. First, the fastest piezoelectric stages have small step response times on the order a few milliseconds. Second, these stages typically have resonant frequencies on the order of 1 kHz when unloaded and down to 500 Hz when loaded. Near these frequencies, the stage position oscillates for even low amplitude signals. To avoid this, control signals are either designed specifically to avoid high frequencies, or a low-pass filter is deliberately inserted into the system to block them.

This simulated tracking system was then used to pinpoint the values of the best control parameters. Different values of $\mathbf{K_P}$ and $\mathbf{K_I}$ were applied to 10 trajectories lasting 1 ms each (100 data points). The integrated squared error between the simulated stage and particle positions was integrated over all ten trajectories and used as an evaluation of the tested parameters. Figure 7 shows the result of testing trajectories for 50 logarithmically spaced values of $\mathbf{K_P}$ and $\mathbf{K_I}$ from 10^{-10} to 10^{-2}, with $\mathbf{K_D}$ being held at zero. As can be clearly seen from the plot, high values of both $\mathbf{K_P}$ and $\mathbf{K_I}$ lead to tracking instability. Interestingly, the empirically found best parameters (shown as the red spot on the plot in Fig. 7) can be seen as a local minimum of the control surface. Within this local minimum, there is relatively little effect of value of $\mathbf{K_P}$ of $\mathbf{K_I}$ on the tracking error. It is also apparent that these empirically derived values lie significantly far from the optimal control parameters, which appear as a "ravine" in the control space (as indicated by the green arrow in Figure 7). These values produce simulated tracking errors which are 10^2 smaller than in the case of the empirical parameters, which could lead to the tracking of much smaller and faster molecules.

To further investigate the behavior of the simulated tracking system under these different control conditions, Figure 8a shows a simulated trajectory for the empirically determined parameters (top) and the ideal parameters (bottom). The empirically determined parameters issue stage commands (green) which closely match the actual particle position (blue). The resulting stage position (red) appears as a smoothed and slightly delayed signal which tracks the particle position. This differs greatly from the newly calculated ideal PID parameters, which drive the stage command with high amplitude such that the stage position almost exactly matches the particle position. The power spectrum of the different control methods shown in Figure 8c gives some insight into the reason that the ideal parameters are not found to be the same as the empirical parameters. Shown in blue is the power spectrum of the diffusive particle, which shows a distinctively Brownian character. The empirical parameters (green) yield a power spectrum which closely matches the particle spectrum, with a small increase in frequencies above 10 kHz. The ideal parameters (red), however, show much higher amplitude signals in the regime beyond 1 kHz. If these parameters are applied to a real stage, which does not behave strictly as a low pass filter, there will be significant ringing and overshoot, leading to poor tracking or even damage to the stage. As such, these calculations would suggest that the response of real-time tracking systems is more dominated by the piezoelectric stage than the optical detection modalities.

The one parameter which is frequently neglected in the experimental case is $\mathbf{K_D}$, as typically no noticeable difference in tracking is observed for any value of $\mathbf{K_D}$. To see if any value of $\mathbf{K_D}$ can be used to improve speed and accuracy in tracking, we simulated the tracking response for 100 values of $\mathbf{K_D}$, logarithmically spaced between 10^{-6} and 10^{6}. As shown in Figure 8d, there is no effect of $\mathbf{K_D}$ on the tracking performance (negative values were also tested). This is not a surprising result, as a diffusing particle is highly random and the next step in the process will have almost no relation to the previous step. Further, derivative

control is notoriously susceptible to noise, which would overwhelm any possible benefit that derivative control might add to this system.

Conclusion and Outlook

In the overarching goal of changing real-time 3D single-particle tracking to real-time 3D single-**molecule** tracking, it is necessary that fast and sensitive detection and feedback mechanisms are found. From the above, it is clear the limiting factor in real-time 3D single-particle tracking is the limited temporal and frequency response of 3D piezoelectric stages. As an illustrative example, Figure 9 shows the mean step size for particles with varying hydrodynamic diameter. The blue curve shows that a 60 nm particle makes a mean step size of ~127 nm in 1 ms. In other words, in this time window a particle can go from the center of the focal volume to the edge between measurements. This is significant because this is the typical response time of a piezoelectric stage and the empirically determined fastest particle that can be tracked by the optical cantilever method has a radius of 60 nm. This strongly suggests that the response time of the stage limits tracking of faster particles. If faster response mechanisms allow an order of magnitude faster response (yellow curve, 0.1 ms step size), this could pave the way to following the behavior of single molecules in aqueous environments, allowing the study of single molecule dynamics in nearly any environment.

Acknowledgment

This work was supported by the US Department of Energy and Princeton University.

References

1 Diaspro, A. (Wiley-Liss, Inc, New York, 2002).
2 Minsky, M. Memoir On Inventing The Confocal Scanning Microscope. *Scanning* **10**, 128-138, (1988).
3 Brakenhoff, G. J., Blom, P., Barends, P. J. & Bakker, C. High-Resolution Confocal Scanning Light-Microscopy. *Ultramicroscopy* **4**, 115-115, (1979).
4 Brakenhoff, G. J., Vandervoort, H. T. M., Vanspronsen, E. A., Linnemans, W. A. M. & Nanninga, N. 3-Dimensional Chromatin Distribution In Neuro-Blastoma Nuclei Shown By Confocal Scanning Laser Microscopy. *Nature* **317**, 748-749, (1985).
5 Sanderson, M. J. & Parker, I. in *Methods Enzymol.* Vol. Volume 360 (ed Ian Parker Gerard Marriott) 447-481 (Academic Press, 2003).
6 Planchon, T. A., Gao, L., Milkie, D. E., Davidson, M. W., Galbraith, J. A., Galbraith, C. G. & Betzig, E. Rapid three-dimensional isotropic imaging of living cells using Bessel beam plane illumination. *Nat. Methods* **8**, 417, (2011).
7 Petran, M., Hadravsk.M, Egger, M. D. & Galambos, R. Tandem-Scanning Reflected-Light Microscope. *Journal Of The Optical Society Of America* **58**, 661-&, (1968).
8 McAllister, R. G., Sisan, D. R. & Urbach, J. S. Design and optimization of a high-speed, high-sensitivity, spinning disk confocal microscopy system. *J. Biomed. Opt.* **13**, (2008).
9 Wang, E., Babbey, C. M. & Dunn, K. W. Performance comparison between the high-speed Yokogawa spinning disc confocal system and single-point scanning confocal systems. *J. Microsc.-Oxford* **218**, 148-159, (2005).
10 Hell, S. & Stelzer, E. H. K. Properties Of A 4pi Confocal Fluorescence Microscope. *Journal Of The Optical Society Of America A-Optics Image Science And Vision* **9**, 2159-2166, (1992).
11 Hell, S. & Stelzer, E. H. K. Fundamental Improvement Of Resolution With A 4pi-Confocal Fluorescence Microscope Using 2-Photon Excitation. *Opt. Commun.* **93**, 277-282, (1992).
12 Klar, T. A., Jakobs, S., Dyba, M., Egner, A. & Hell, S. W. Fluorescence microscopy with diffraction resolution barrier broken by stimulated emission. *Proc. Natl. Acad. Sci. U. S. A.* **97**, 8206-8210, (2000).
13 Schwentker, M. A., Bock, H., Hofmann, M., Jakobs, S., Bewersdorf, J., Eggeling, C. & Hell, S. W. Wide-field subdiffraction RESOLFT microscopy using fluorescent protein photoswitching. *Microsc. Res. Tech.* **70**, 269-280, (2007).

14 Schmidt, R., Wurm, C. A., Punge, A., Egner, A., Jakobs, S. & Hell, S. W. Mitochondrial Cristae Revealed with Focused Light. *Nano Lett.* **9**, 2508-2510, (2009).

15 Westphal, V., Rizzoli, S. O., Lauterbach, M. A., Kamin, D., Jahn, R. & Hell, S. W. Video-rate far-field optical nanoscopy dissects synaptic vesicle movement. *Science* **320**, 246-249, (2008).

16 Bergermann, F., Alber, L., Sahl, S. J., Engelhardt, J. & Hell, S. W. 2000-fold parallelized dual-color STED fluorescence nanoscopy. *Opt. Express* **23**, 211-223, (2015).

17 Chmyrov, A., Keller, J., Grotjohann, T., Ratz, M., d'Este, E., Jakobs, S., Eggeling, C. & Hell, S. W. Nanoscopy with more than 100,000 'doughnuts'. *Nat Meth* **10**, 737-740, (2013).

18 Thompson, R. E., Larson, D. R. & Webb, W. W. Precise Nanometer Localization Analysis for Individual Fluorescent Probes. *Biophys. J.* **82**, 2775, (2002).

19 Yildiz, A., Forkey, J. N., McKinney, S. A., Ha, T., Goldman, Y. E. & Selvin, P. R. Myosin V walks hand-over-hand: Single fluorophore imaging with 1.5-nm localization. *Science* **300**, 2061-2065, (2003).

20 Rust, M. J., Bates, M. & Zhuang, X. Sub-diffraction-limit imaging by stochastic optical reconstruction microscopy (STORM). *Nat. Methods* **3**, 793-796, (2006).

21 Betzig, E., Patterson, G. H., Sougrat, R., Lindwasser, O. W., Olenych, S., Bonifacino, J. S., Davidson, M. W., Lippincott-Schwartz, J. & Hess, H. F. Imaging Intracellular Fluorescent Proteins at Nanometer Resolution. *Science* **313**, 1642-1645, (2006).

22 Hess, S. T., Girirajan, T. P. K. & Mason, M. D. Ultra-high resolution imaging by fluorescence photoactivation localization microscopy. *Biophys. J.* **91**, 4258-4272, (2006).

23 Huang, B., Wang, W., Bates, M. & Zhuang, X. Three-Dimensional Super-Resolution Imaging by Stochastic Optical Reconstruction Microscopy. *Science* **319**, 810-813, (2008).

24 Jones, S. A., Shim, S. H., He, J. & Zhuang, X. W. Fast, three-dimensional super-resolution imaging of live cells. *Nat. Methods* **8**, 499-505, (2011).

25 Juette, M. F., Gould, T. J., Lessard, M. D., Mlodzianoski, M. J., Nagpure, B. S., Bennett, B. T., Hess, S. T. & Bewersdorf, J. Three-dimensional sub-100 nm resolution fluorescence microscopy of thick samples. *Nat. Methods* **5**, 527-529, (2008).

26 Shtengel, G., Galbraith, J. A., Galbraith, C. G., Lippincott-Schwartz, J., Gillette, J. M., Manley, S., Sougrat, R., Waterman, C. M., Kanchanawong, P., Davidson, M. W., Fetter, R. D. & Hess, H. F. Interferometric fluorescent super-resolution microscopy resolves 3D cellular ultrastructure. *Proc. Natl. Acad. Sci. U. S. A.* **106**, 3125-3130, (2009).

27 Thompson, M. A., Lew, M. D., Badieirostami, M. & Moerner, W. E. Localizing and Tracking Single Nanoscale Emitters in Three Dimensions with High Spatiotemporal Resolution Using a Double-Helix Point Spread Function. *Nano Lett.* **10**, 211-218, (2010).

28 Badieirostami, M., Lew, M. D., Thompson, M. A. & Moerner, W. E. Three-dimensional localization precision of the double-helix point spread function versus astigmatism and biplane. *Appl. Phys. Lett.* **97**, (2010).

29 Shechtman, Y., Weiss, L. E., Backer, A. S., Sahl, S. J. & Moerner, W. E. Precise 3D scan-free multiple-particle tracking over large axial ranges with Tetrapod point spread functions. *Nano Lett.*, (2015).

30 Zhu, L., Zhang, W., Elnatan, D. & Huang, B. Faster STORM using compressed sensing. *Nat Meth* **9**, 721-723, (2012).

31 Shim, S.-H., Xia, C., Zhong, G., Babcock, H. P., Vaughan, J. C., Huang, B., Wang, X., Xu, C., Bi, G.-Q. & Zhuang, X. Super-resolution fluorescence imaging of organelles in live cells with photoswitchable membrane probes. *Proceedings of the National Academy of Sciences* **109**, 13978-13983, (2012).

32 Huang, F., Hartwich, T. M. P., Rivera-Molina, F. E., Lin, Y., Duim, W. C., Long, J. J., Uchil, P. D., Myers, J. R., Baird, M. A., Mothes, W., Davidson, M. W., Toomre, D. & Bewersdorf, J. Video-rate nanoscopy using sCMOS camera-specific single-molecule localization algorithms. *Nat Meth* **10**, 653-658, (2013).

33 Huisken, J., Swoger, J., Del Bene, F., Wittbrodt, J. & Stelzer, E. H. K. Optical sectioning deep inside live embryos by selective plane illumination microscopy. *Science* **305**, 1007-1009, (2004).

34 Holekamp, T. F., Turaga, D. & Holy, T. E. Fast three-dimensional fluorescence imaging of activity in neural populations by objective-coupled planar illumination microscopy. *Neuron* **57**, 661-672, (2008).

35 Keller, P. J., Schmidt, A. D., Wittbrodt, J. & Stelzer, E. H. K. Reconstruction of Zebrafish Early Embryonic Development by Scanned Light Sheet Microscopy. *Science* **322**, 1065-1069, (2008).

36 Keller, P. J., Schmidt, A. D., Santella, A., Khairy, K., Bao, Z., Wittbrodt, J. & Stelzer, E. H. K. Fast, high-contrast imaging of animal development with scanned light sheet-based structured-illumination microscopy. *Nat. Methods* **7**, 637-U655, (2010).

37 Bouchard, M. B., Voleti, V., Mendes, C. S., Lacefield, C., Grueber, W. B., Mann, R. S., Bruno, R. M. & Hillman, E. M. C. Swept confocally-aligned planar excitation (SCAPE) microscopy for high-speed volumetric imaging of behaving organisms. *Nat. Photonics* **9**, 113-119, (2015).

38 Gao, L., Shao, L., Higgins, Christopher D., Poulton, John S., Peifer, M., Davidson, Michael W., Wu, X., Goldstein, B. & Betzig, E. Noninvasive Imaging beyond the Diffraction Limit of 3D Dynamics in Thickly Fluorescent Specimens. *Cell* **151**, 1370-1385, (2012).

39 Gustafsson, M. G. L. Surpassing the lateral resolution limit by a factor of two using structured illumination microscopy. *J. Microsc.-Oxford* **198**, 82-87, (2000).

40 Schermelleh, L., Carlton, P. M., Haase, S., Shao, L., Winoto, L., Kner, P., Burke, B., Cardoso, M. C., Agard, D. A., Gustafsson, M. G. L., Leonhardt, H. & Sedat, J. W. Subdiffraction multicolor imaging of the nuclear periphery with 3D structured illumination microscopy. *Science* **320**, 1332-1336, (2008).

41 Shao, L., Kner, P., Rego, E. H. & Gustafsson, M. G. L. Super-resolution 3D microscopy of live whole cells using structured illumination. *Nat. Methods* **8**, 1044, (2011).

42 York, A. G., Chandris, P., Nogare, D. D., Head, J., Wawrzusin, P., Fischer, R. S., Chitnis, A. & Shroff, H. Instant super-resolution imaging in live cells and embryos via analog image processing. *Nat Meth* **10**, 1122-1126, (2013).

43 Lessard, G. A., Goodwin, P. M. & Werner, J. H. Three-dimensional tracking of individual quantum dots. *Appl. Phys. Lett.* **91**, (2007).

44 McHale, K., Berglund, A. J. & Mabuchi, H. Quantum Dot Photon Statistics Measured by Three-Dimensional Particle Tracking. *Nano Lett.* **7**, 3535-3539, (2007).

45 Cang, H., Xu, C. S., Montiel, D. & Yang, H. Guiding a confocal microscope by single fluorescent nanoparticles. *Opt. Lett.* **32**, 2729-2731, (2007).

46 Cang, H., Wong, C. M., Xu, C. S., Rizvi, A. H. & Yang, H. Confocal three dimensional tracking of a single nanoparticle with concurrent spectroscopic readouts. *Appl. Phys. Lett.* **88**, 223901, (2006).

47 Welsher, K. & Yang, H. Multi-resolution 3D visualization of the early stages of cellular uptake of peptide-coated nanoparticles. *Nat. Nanotechnol.* **9**, 198-203, (2014).

48 Console, S., Marty, C., García-Echeverría, C., Schwendener, R. & Ballmer-Hofer, K. Antennapedia and HIV Transactivator of Transcription (TAT) "Protein Transduction Domains" Promote Endocytosis of High Molecular Weight Cargo upon Binding to Cell Surface Glycosaminoglycans. *J. Biol. Chem.* **278**, 35109-35114, (2003).

49 Wells, N. P., Lessard, G. A., Goodwin, P. M., Phipps, M. E., Cutler, P. J., Lidke, D. S., Wilson, B. S. & Werner, J. H. Time-Resolved Three-Dimensional Molecular Tracking in Live Cells. *Nano Lett.* **10**, 4732-4737, (2010).

50 Han, J. J., Kiss, C., Bradbury, A. R. M. & Werner, J. H. Time-Resolved, Confocal Single-Molecule Tracking of Individual Organic Dyes and Fluorescent Proteins in Three Dimensions. *ACS Nano* **6**, 8922-8932, (2012).

51 Katayama, Y., Burkacky, O., Meyer, M., Bräuchle, C., Gratton, E. & Lamb, D. C. Real-Time Nanomicroscopy via Three-Dimensional Single-Particle Tracking. *ChemPhysChem* **10**, 2458-2464, (2009).

52 Kiam Heong, A., Chong, G. & Yun, L. PID control system analysis, design, and technology. *Control Systems Technology, IEEE Transactions on* **13**, 559-576, (2005).

Figure Captions

Figure 1. Spatiotemporal resolution of common imaging methods. Each rectangle represents the spatial and temporal precision of a 3D imaging method. The left bound of each rectangle represents the spatial precision of each method. In the case of methods where there is anisotropy between lateral and axial resolution (as is commonly the case), the worse of the two is plotted. The right edge of each rectangle represents the maximum spatial scale each method can address. Again, the smaller of the lateral and axial scale is plotted. On the temporal axis, the bottom of each rectangle represents the fastest imaging rate for each method in 3D for the given spatial precision and scale. While the spatial scales along the x-axis have been fully covered, it has been done at the expense of temporal precision, as demonstrated by the lack of methods that can reach time scales below 10 ms.

Figure 2. Imaging rates versus spatial scale. For all imaging methods, there is a trade-off between the maximum spatial scale that can be addressed and the imaging or frame rate. This is most obvious in the case of point scanning methods such as LSM or STED. The plot shows the relationship between maximum spatial scale addressed, pixel dwell time and the overall imaging rates. When imaging volumes on the 10s of micron scale, the highest achievable rates are on the order of 1 volume per second (VPS), even with a pixel dwell time of 1 μsec. As the spatial scale and pixel dwell time are reduced, the imaging rate increases exponentially. This implies that to achieve the highest possible measurement rates, it is necessary to minimize both the pixel integration time and the spatial scale addressed, which is exactly what real-time 3D single-particle tracking achieves.

Figure 3. 3D-MM measurement of a membrane bound nanoparticle. (A) 100 nm TAT labeled fluorescent nanoparticles were tracked along the 3D cellular surface using the 3D-MM method. The nanoparticles were allowed to bind to NIH-3T3 cells expressing cytosolic GFP and CFP NLS, which served as labels for the 2P-LSM readout. The green surfaces represent the extent of the cytosol, while the blue surface shows the nucleus. The black arrow shows the location of the 3D nanoparticle trajectory within the 70 μm x 70 μm x 4 μm field of view. **(B)** Zoom in of the 3D-MM trajectory in (A), showing the particle diffusing along the membrane. As the particle diffuses, it traces out 3D structures such as hemispherical (blue arrow) and cylindrical (red arrow) protrusions. **(C)** Edge-on view of the particle diffusing along the membrane surface, with multiple membrane features resolved by the particle's trajectory. **(D)** Zoom in on a cylindrical protrusion of ~250 nm in diameter carved out by the diffusing nanoparticle. Note the high precision of the real-time 3D tracking is converted into a high-resolution structure by integrating the oversampled position over long times.

Figure 4. The optical cantilever. The cartoon inset demonstrates the mechanism of the optical cantilever. As a particle is displaced in the object plane, the output light collected by the objective exits the back focal plane at an angle determined by the focal length of the lens. This infinity space light is then projected onto a prism mirror which splits the light onto two detectors. The angular deviation of the beam leads to displacement of the center of the beam at the prism mirror and this displacement is linearly proportional to the distance between the back focal plane of the lens and the prism mirror, which is referred to as the optical cantilever. The plot shows the simulated response of the normalized difference of two detectors as a function of particle displacement in the object plane for different optical cantilever lengths. For short lengths (100 mm), the response is linear over a long range, but has low sensitivity to particle displacement. For long lengths (100 m), the response becomes very steep, but is only linear over about 8 nm. The ideal response occurs for cantilever lengths on the order of a few meters.

Figure 5. Calculated versus experimental response curves of a 2 m optical cantilever. The experimental response of a 2 m optical cantilever was measured by scanning a 110 nm fluorescent nanoparticle through the focal volume of a 100x objective lens ($\mathbf{f_{obj}}$ = 1.65 mm). Following the optical cantilever ($\mathbf{f_{tube}}$ = 200 mm, $\mathbf{f_{cantilever}}$ = 75 mm, L = 2 m) the emission light is split by a prism mirror onto two single-photon counting APDs. The normalized difference of the intensities of the two detectors are calculated as a function of particle position. The calculated (red line) and measured (green circles) responses of the system are in remarkably good agreement.

Figure 6. The offset pinhole enables high resolution Z tracking. A short focal length lens (f = 2.9 mm) is used to image the target particle onto a pinhole. The plot shows the relative light intensity collected by a detector immediately after the pinhole normalized to the light collected for XY tracking. The size of the pinhole and offset from the XY focal volume affects both the steepness and range of control allowed, with a 10 μm pinhole providing a compromise between the two factors. The purple circles show the results of a fluorescent nanoparticle scanned through the tracking volume and detected with the 10 μm offset pinhole, showing good agreement with the predicted behavior.

Figure 7. PID tuning for optical tracking response. The effect of different values of $\mathbf{K_P}$ and $\mathbf{K_I}$ were simulated by tracking a 60 nm nanoparticle undergoing a Brownian random walk in one dimension. The optical response was taken from the data in Figure 4, while the stage response was modeled as a 500 Hz low pass filter. The plot shows the empirically derived values (red region) lie in a local minimum, which is relatively flat. The plot also reveals a global minimum in tracking error at a critical value of $\mathbf{K_P}$ that is relatively independent of $\mathbf{K_I}$ (green arrow).

Figure 8. Simulated 1D tracking for empirically derived and ideal PID parameters. (A) Tracking was simulated for empirically derived (top) as well as "ideal" (bottom) PID parameters as found in Figure 5. For the empirical parameters, the tracked stage position (red) is smoothed relative to the actual particle position (blue), while for the ideal parameters, the tracked stage position almost identically matches the particle position. **(B)** Zoom in of the trajectories shown in (A). The empirical tracking (top, red curve) is smoothed and delayed relative to the particle position (top, blue curve). In the case of the ideal parameters (bottom), the stage control (green) is driven with high frequency and high amplitude to match the particle's position. **(C)** Power spectrum of the simulated particle position (blue), empirical PID stage commands (green) and ideal PID stage commands (red). The empirical PID parameters closely follow the frequency response of the particle itself, avoiding high frequencies which lead to overshoot and ringing in the piezoelectric stage. The ideal parameters show large amplitude high frequency components above the piezoelectric stage resonant frequency (~ 1 kHz). **(D)** Evaluation of the effect of $\mathbf{K_D}$ on simulated trajectories, showing that no value has a significant effect on the tracking error.

Figure 9. Mean step size versus response time. The blue curve shows the mean diffusive step size expected at 1 ms delay for Brownian diffusion. The red circle highlights that for a 60 nm particle this step size is ~127 nm, on the order of the radius of the PSF of a 100x objective lens. The yellow curve shows that if the response time of the system can be reduced to 0.1 ms, the expected step size can be maintained below this cut-off for all particle diameters, even down to the scale of single molecules.

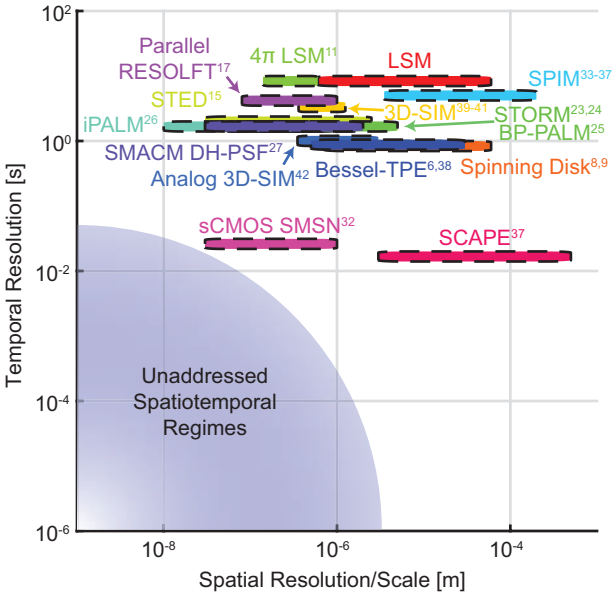
Parallel RESOLFT[17]
4π LSM[11]
LSM
SPIM[33-37]
STED[15]
3D-SIM[39-41]
STORM[23,24]
iPALM[26]
BP-PALM[25]
SMACM DH-PSF[27]
Analog 3D-SIM[42]
Bessel-TPE[6,38]
Spinning Disk[8,9]
sCMOS SMSN[32]
SCAPE[37]
Unaddressed Spatiotemporal Regimes
Temporal Resolution [s]
Spatial Resolution/Scale [m]
10^2
10^0
10^-2
10^-4
10^-6
10^-8
10^-6
10^-4

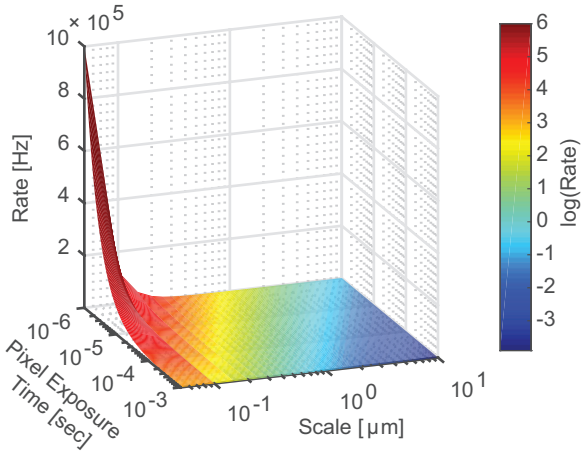
× 10^5
10
8
6
4
2
Rate [Hz]
10^-6
10^-5
10^-4
10^-3
Pixel Exposure Time [sec]
10^-1
10^0
10^1
Scale [µm]
6
5
4
3
2
1
0
-1
-2
-3
log(Rate)

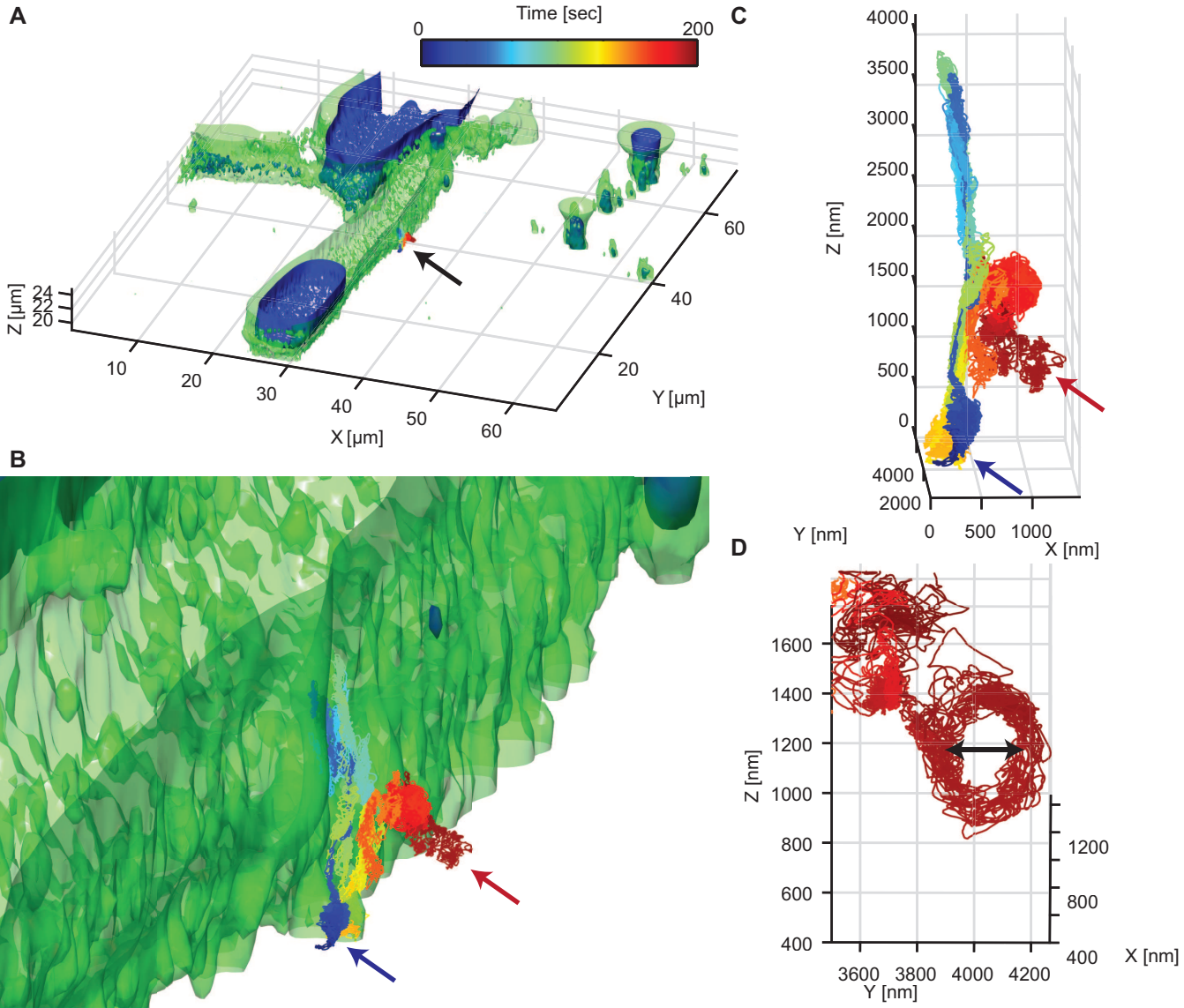
A
Time [sec]
0
200
Z [µm]
24
22
20
10
20
30
40
50
60
X [µm]
20
40
60
Y [µm]
B
C
4000
3500
3000
2500
2000
1500
1000
500
0
Z [nm]
4000
2000
Y [nm]
0
500
1000
X [nm]
D
1600
1400
1200
1000
800
600
400
Z [nm]
3600
3800
4000
4200
Y [nm]
1200
800
400
X [nm]

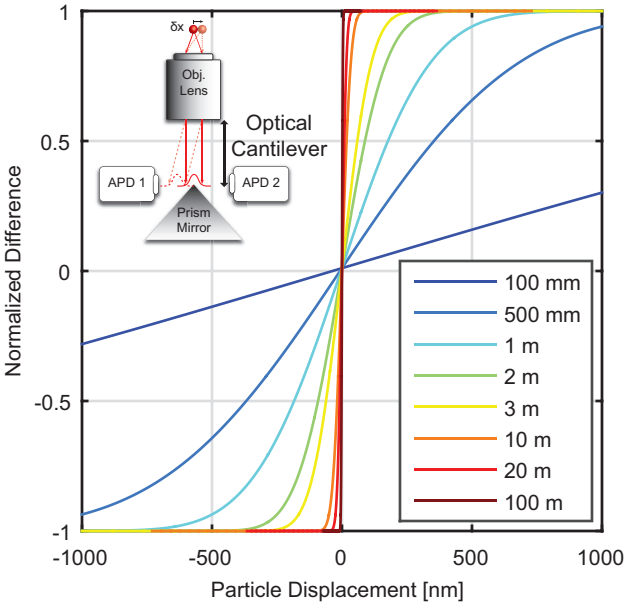
δx
Obj. Lens
Optical Cantilever
APD 1
APD 2
Prism Mirror
100 mm
500 mm
1 m
2 m
3 m
10 m
20 m
100 m
Normalized Difference
Particle Displacement [nm]
1
0.5
0
-0.5
-1
-1000
-500
0
500
1000

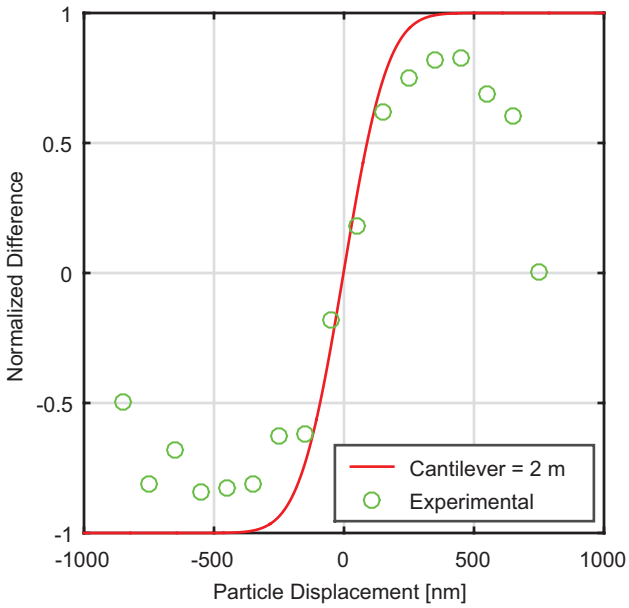
1
0.5
0
-0.5
-1
-1000
-500
0
500
1000
Normalized Difference
Particle Displacement [nm]
Cantilever = 2 m
Experimental

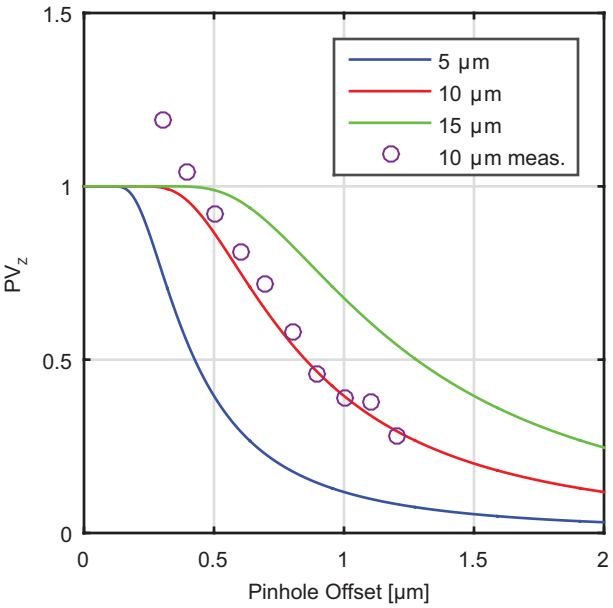
1.5
1
0.5
0
0
0.5
1
1.5
2
PV_z
Pinhole Offset [µm]
5 µm
10 µm
15 µm
10 µm meas.

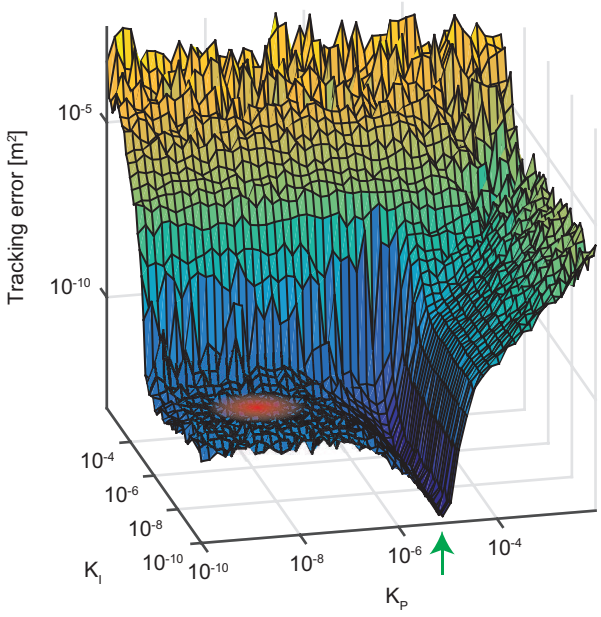
Tracking error [m²]
10-5
10-10
10-4
10-6
10-8
10-10
KI
10-10
10-8
10-6
10-4
KP

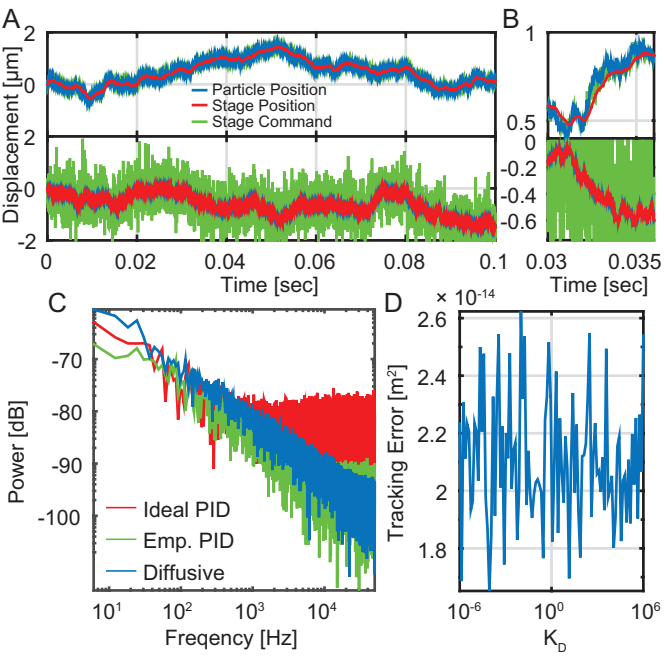
A
B
C
D
Displacement [μm]
Particle Position
Stage Position
Stage Command
Time [sec]
Time [sec]
Power [dB]
Ideal PID
Emp. PID
Diffusive
Freqency [Hz]
Tracking Error [m²]
× 10⁻¹⁴
K_D

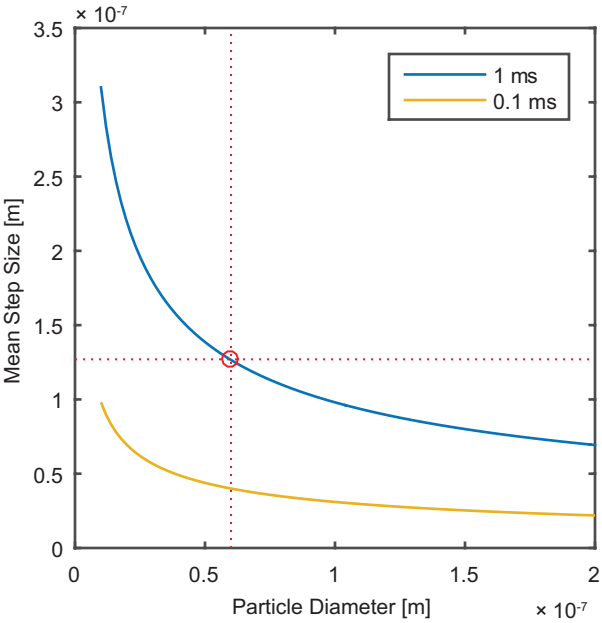
× 10-7
3.5
3
2.5
2
1.5
1
0.5
0
1 ms
0.1 ms
Mean Step Size [m]
0
0.5
1
1.5
2
Particle Diameter [m]
× 10-7